Adaptive Optics Retinal Imaging in *CNGA3*-Associated Achromatopsia: Retinal Characterization, Interocular Symmetry, and Intrafamilial Variability

Michalis Georgiou,[1,2] Katie M. Litts,[3] Angelos Kalitzeos,[1,2] Christopher S. Langlo,[3] Thomas Kane,[1,2] Navjit Singh,[1,2] Melissa Kassilian,[1,2] Nashila Hirji,[1,2] Neruban Kumaran,[1,2] Alfredo Dubra,[4] Joseph Carroll,[3] and Michel Michaelides[1,2]

[1]UCL Institute of Ophthalmology, University College London, London, United Kingdom
[2]Moorfields Eye Hospital NHS Foundation Trust, City Road, London, United Kingdom
[3]Department of Ophthalmology & Visual Sciences, Medical College of Wisconsin, Milwaukee, Wisconsin, United States
[4]Department of Ophthalmology, Stanford University, Palo Alto, California, United States

PURPOSE. To investigate retinal structure in subjects with *CNGA3*-associated achromatopsia and evaluate disease symmetry and intrafamilial variability.

METHODS. Thirty-eight molecularly confirmed subjects underwent ocular examination, optical coherence tomography (OCT), and nonconfocal split-detection adaptive optics scanning light ophthalmoscopy (AOSLO). OCT scans were used for evaluating foveal hypoplasia, grading foveal ellipsoid zone (EZ) disruption, and measuring outer nuclear layer (ONL) thickness. AOSLO images were used to quantify peak foveal cone density, intercell distance (ICD), and the coefficient of variation (CV) of ICD.

RESULTS. Mean ($\pm$SD) age was 25.9 ($\pm$13.1) years. Mean ($\pm$ SD) best corrected visual acuity (BCVA) was 0.87 ($\pm$0.14) logarithm of the minimum angle of resolution. Examination with OCT showed variable disruption or loss of the EZ. Seven subjects were evaluated for disease symmetry, with peak foveal cone density, ICD, CV, ONL thickness, and BCVA not differing significantly between eyes. A cross-sectional evaluation of AOSLO imaging showed a mean ($\pm$SD) peak foveal cone density of 19,844 ($\pm$13,046) cones/mm^2. There was a weak negative association between age and peak foveal cone density ($r = -0.397$, $P = 0.102$), as well as between EZ grade and age ($P = 0.086$).

CONCLUSIONS. The remnant cone mosaics were irregular and variably disrupted, with significantly lower peak foveal cone density than unaffected individuals. Variability was also seen among subjects with identical mutations. Therefore, subjects should be considered on an individual basis for stratification in clinical trials. Interocular symmetry suggests that both eyes have comparable therapeutic potential and the fellow eye can serve as a valid control. Longitudinal studies are needed, to further examine the weak negative association between age and foveal cone structure observed here.

Keywords: adaptive optics, retinal phenotyping, retinal diseases, inherited retinal diseases, genetics, *CNGA3*, cone, cone dysfunction, achromatopsia

Achromatopsia (ACHM) presents from birth or early infancy, with poor visual acuity, pendular nystagmus, photophobia, and color vision loss in all three axes.[1,2] Absent cone electroretinogram responses is the hallmark of disease, with normal rod function or uncommonly mildly reduced rod responses.[3–5] ACHM is an autosomal recessive disorder with a heterogeneous genetic background. Disease-causing sequence variants have been reported in *CNGA3* (ACHM2, Online Mendelian Inheritance in Man [OMIM] 600053),[6,7] *CNGB3* (ACHM3, OMIM 605080),[8] *GNAT2* (ACHM4, OMIM 139340),[9,10] *ATF6* (ACHM7, OMIM 616517),[11] *PDE6H* (ACHM6, OMIM I610024),[12] and *PDE6C* (ACHM5, OMIM 600827).[1]

CNGA3 encodes the α subunit of the cGMP-gated cation channel,[13] located in cone outer segments, categorizing *CNGA3*-associated ACHM as a "channelopathy."[14] It has been shown in vitro that α subunits can create functional channels in the absence of β subunits, a property not shared by the β subunits.[15] *CNGA3* variants have a far greater allelic heterogeneity than *CNGB3*.[16,17] In a large cross-sectional study of *CNGA3*-ACHM ($n = 36$), Zobor et al.[18] reported a lack of robust association between age and morphologic (optical coherence tomography [OCT]) and/or functional (microperimetry) changes, in agreement with a previous cross-sectional study of ACHM by Sundaram et al.[19] ($n = 40$, with 18 having *CNGA3*-ACHM). Aboshiha et al.,[20] in a prospective longitudinal study ($n = 40$, with 18 having *CNGA3*-ACHM) using OCT and fundus autofluorescence imaging, identified a slow and subtle progression of disease in a minority of subjects. These studies were limited by the relatively low resolution of the imaging tools used.

Adaptive optics (AO) has been used for in-depth phenotyping in inherited retinal diseases for two decades,[21] by allowing
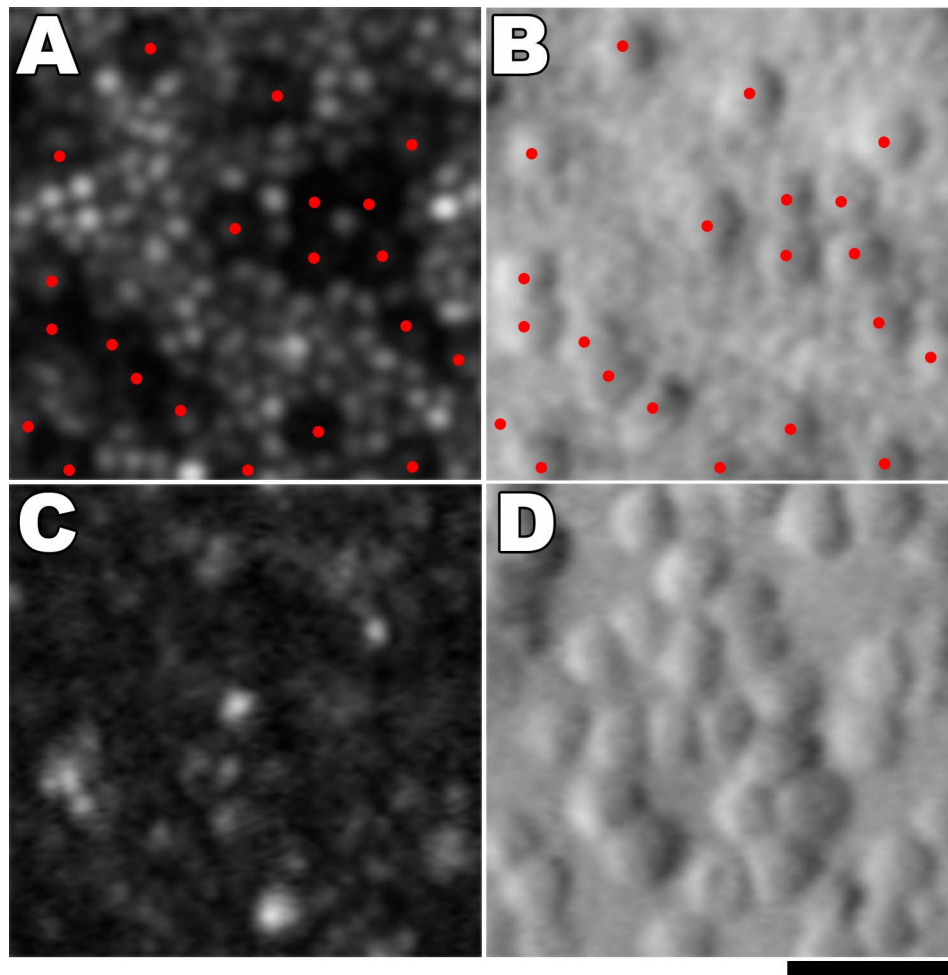
FIGURE 1. Adaptive optics scanning light ophthalmoscopy imaging in *CNGA3*-associated ACHM. At 2° eccentricity: (**A**) confocal image, with *red dots* marking the dark cones. Cones are surrounded by waveguiding rods. (**B**) Split-detection image over the exact same region with overlying *red dots* showing the cones marked in panel **A**, which colocalize with cone inner segments, surrounded by rods. Foveal center: (**C**) confocal image at the foveal center, where the dark cones are not visible because no rods are present to delineate the dark spaces. (**D**) Split-detection image over the exact same region, with visible and quantifiable cone inner segments. All images are from the same retinal montage. *Scale bar*: 20 μm.

the noninvasive visualization of the photoreceptor mosaic[22–24] through the correction of the eye's monochromatic aberrations.[24,25] Confocal detection of reflected light has been shown to reflect the waveguiding ability of intact photoreceptors.[23,26,27] Early investigations in ACHM with flood illumination-AO and confocal adaptive optics scanning light ophthalmoscopy (AOSLO) identified dark spaces in the cone mosaic, increased cone spacing, and/or decreased cone density (Fig. 1A).[28–31] Marked variability in the cone mosaic has been observed across individuals; while no obvious difference has been reported between the two most common genotypes (*CNGA3* and *CNGB3*), the rarer *GNAT2* genotype is associated with a significantly less-disrupted photoreceptor mosaic.[30,32] Reduced reflectivity (i.e., altered waveguiding) in the majority of remnant cones in *CNGA3* and *CNGB3* has also been noted, with relative preservation in *GNAT2*.[30] Until the advent of nonconfocal split-detection AOSLO, it was unknown if these dark spaces harbored nonwaveguiding cones or indicated the loss of cones, an important question for defining the presence of a therapeutic target. Simultaneous confocal and split-detection AOSLO has allowed for the identification of cone inner segment structure in these spaces (Fig. 1B)[33–36] and transformed our understanding of ACHM and participant selection for planned and ongoing *CNGA3*- and *CNGB3*-ACHM

gene therapy trials. In confocal AOSLO imaging outside the foveal center, due to waveguiding rods surrounding the nonreflective dark cones, the cones can be identified (Fig. 1A). This is in contrast to the fovea, where the lack of surrounding rods makes the identification and quantification of cones impossible (Fig. 1C) and split-detection AOSLO is necessary (Fig. 1D). Given the potential disconnect between OCT and AOSLO measures of cone integrity[37] and the ability of AOSLO to directly visualize the target cones for gene replacement, nonconfocal split-detection AOSLO imaging is the modality of choice to identify patients most likely to benefit from cone-directed rescue.

The current literature for *CNGA3*-ACHM and split-detection AOSLO imaging is limited, with most studies focusing on the more common *CNGB3* phenotype and/or only using confocal AOSLO. The purpose of this study was to use OCT and split-detection AOSLO to explore the structural phenotype of patients with molecularly-confirmed *CNGA3*-ACHM, and lay the groundwork for a *CNGA3* longitudinal AOSLO study to define the cellular natural history of this disorder, in light of the ongoing and upcoming gene therapy trials. In addition, we examined disease symmetry at the cellular level and investigated intrafamilial variability. We compared our observations

with published *CNGB3*-ACHM data obtained using similar methodology.[36]

MATERIALS AND METHODS

The study was approved by the Ethics Committees of Moorfields Eye Hospital and the Medical College of Wisconsin. Written informed consent was obtained from all subjects after explanation of the nature and possible consequences of the study. The research followed the tenets of the Declaration of Helsinki.

Participants

Thirty-eight ACHM subjects with likely disease-causing sequence variants in *CNGA3* were recruited from Moorfields Eye Hospital, London, UK, and the Medical College of Wisconsin, Milwaukee, USA.

Ocular Examination

A full clinical history assessment and ocular examination was carried out in 32 of the subjects, including best corrected visual acuity (BCVA) using the Early Treatment Diabetic Retinopathy Study chart. Axial length was obtained with the Zeiss IOLMaster (Carl Zeiss Meditec, Jena, Germany) in order to scale the AOSLO retinal images and the OCT scans for all subjects.

Optical Coherence Tomography (OCT)

All subjects were imaged using the Bioptigen spectral domain OCT (Leica Microsystems, Research Triangle Park, NC, USA) bilaterally. Pupil dilation and cycloplegia were achieved by instilling one drop of phenylephrine hydrochloride (2.5%) and tropicamide (1%) in each eye prior to imaging (OCT/AOSLO). The scanning window covered a nominal 7×7-mm retinal area and vertical and horizontal scans centered at the fovea with a nominal 7-mm scan length (120 B scans) were recorded. In order to increase the signal-to-noise ratio, the maximum number ($n > 5$) of line scans including the fovea were aligned, registered, and averaged using ImageJ and the StackReg plugin (National Institutes of Health).[38]

The outer nuclear layer (ONL) thickness was calculated at the fovea for all subjects based on the longitudinal reflectivity profile (LRP), as described by Huang et al.[39] The LRP was 5 pixels wide and positioned at the center of the foveal depression, and the foveal ONL thickness was calculated as the distance between the hyperreflective peaks of the posterior outer plexiform layer and external limiting membrane for subjects with foveal hypoplasia. In subjects with normal foveal excavation, the ONL thickness was measured as the distance between the hyperreflective peaks corresponding to the internal limiting membrane and the external limiting membrane. A similar approach has been used in several ACHM studies.[19,36,40]

The transfoveal line scans were then categorized into five grades according to the previously reported grading system by Sundaram et al.,[19] based upon the integrity of the ellipsoid zone (EZ): (1) continuous EZ, (2) EZ disruption, (3) EZ absence, (4) presence of a hyporeflective zone (HRZ), and (5) outer retinal atrophy including retinal pigment epithelium (RPE) loss (Fig. 2). This grading allows meaningful comparisons with other recently published ACHM cohorts.[18,36] The nomenclature used follows the International Nomenclature for Optical Coherence Tomography Consensus.[41] Confirmation of the aforementioned grading was established by examining additional OCT scans acquired using the Spectralis spectral domain OCT system (Heidelberg Engineering Inc., Heidelberg, Germany). The grading was done by two observers independently (MG, CSL) and any discrepancies were resolved with consensus from a third grader (NH). The scans were also examined for the presence of foveal hypoplasia, defined as the presence of one or more inner retinal layers at the foveal center.[19] Both eyes were imaged for each subject, though one eye was chosen randomly for quantitative analysis (except for EZ grade and hypoplasia, which were assessed bilaterally).

AOSLO Imaging of the Photoreceptor Mosaic

All subjects were imaged using one of two identical AOSLO systems, as previously described,[42] at Moorfields Eye Hospital, London, United Kingdom, and the Medical College of Wisconsin, Milwaukee, United States. Imaging with confocal and split-detector modes was performed, with simultaneous acquisition, in absolute spatial and temporal registration. Split-detection AOSLO allows for the visualization of cone inner segments in ACHM based on a differential phase technique.[33]

The imaging light source was a 790-nm super-luminescent diode (SLD; Superlum, Carrigtohill, Cork, Ireland). Image sequences were recorded as AVI files, of 150 frames, either at 1° and/or 1.5° square field of view (FOV). A desinusoiding algorithm was applied to each image sequence and individual frames were selected,[43] registered,[44] and averaged to increase the signal-to-noise ratio for subsequent analysis. Images were obtained over the fovea. The final images were combined into a single montage (Adobe Photoshop, Adobe Systems Inc., San Jose, CA, USA), with images from each modality overlaid on one another, manually and/or using a custom-built automated software.[45] Images taken with a 1° FOV were analyzed preferentially, due to the higher resolution.

The scale in degrees per pixel of each FOV was determined using a Ronchi ruling of known spacing after each imaging session. Then, the value was linearly scaled using the subject's axial length and the final micron per pixel scale was obtained by multiplying by the retinal magnification factor of 291 μm/degree. The AOSLO montages were aligned to color fundus images and OCT images using common blood vessel patterns (Adobe Photoshop). The position of the anatomic foveal center was estimated on the AOSLO images using the aligned OCT images. The rod-free area surrounding the foveal center was used for further AOSLO analysis.

The eligibility criteria for AOSLO analysis were strict; low-quality images (due to involuntary eye motion/nystagmus or low signal-to-noise ratio), noncontiguous montages, and montages not covering the entire rod-free area were excluded from further analysis.

In some subjects ($n = 7$), bilateral AOSLO images were available for evaluating disease symmetry. The low number of subjects with adequate bilateral data was either due to time constraints or incomplete imaging of the fovea, in the second eye. For each subject, the eye with the better image quality (least eye motion, higher signal-to-noise ratio), was selected for cross-sectional evaluation of AOSLO data.

Cone coordinates from every given foveal image were extracted following manual annotation by a single grader (MG). The coordinate arrays were used to assess the peak foveal cone density (cones/mm^2). A 55×55-μm sampling window was used to determine the density at each pixel of the coordinate array. The pixel location with the greatest value was the location of peak foveal cone density, by dividing the total number of cones by the area. In addition, the mean intercell distance (ICD, defined as the average distance of a cone from all its immediate neighbors) and its coefficient of variation (CV, defined as the standard deviation of ICD divided by the mean of ICD) were calculated for the rod-free area for all subjects with
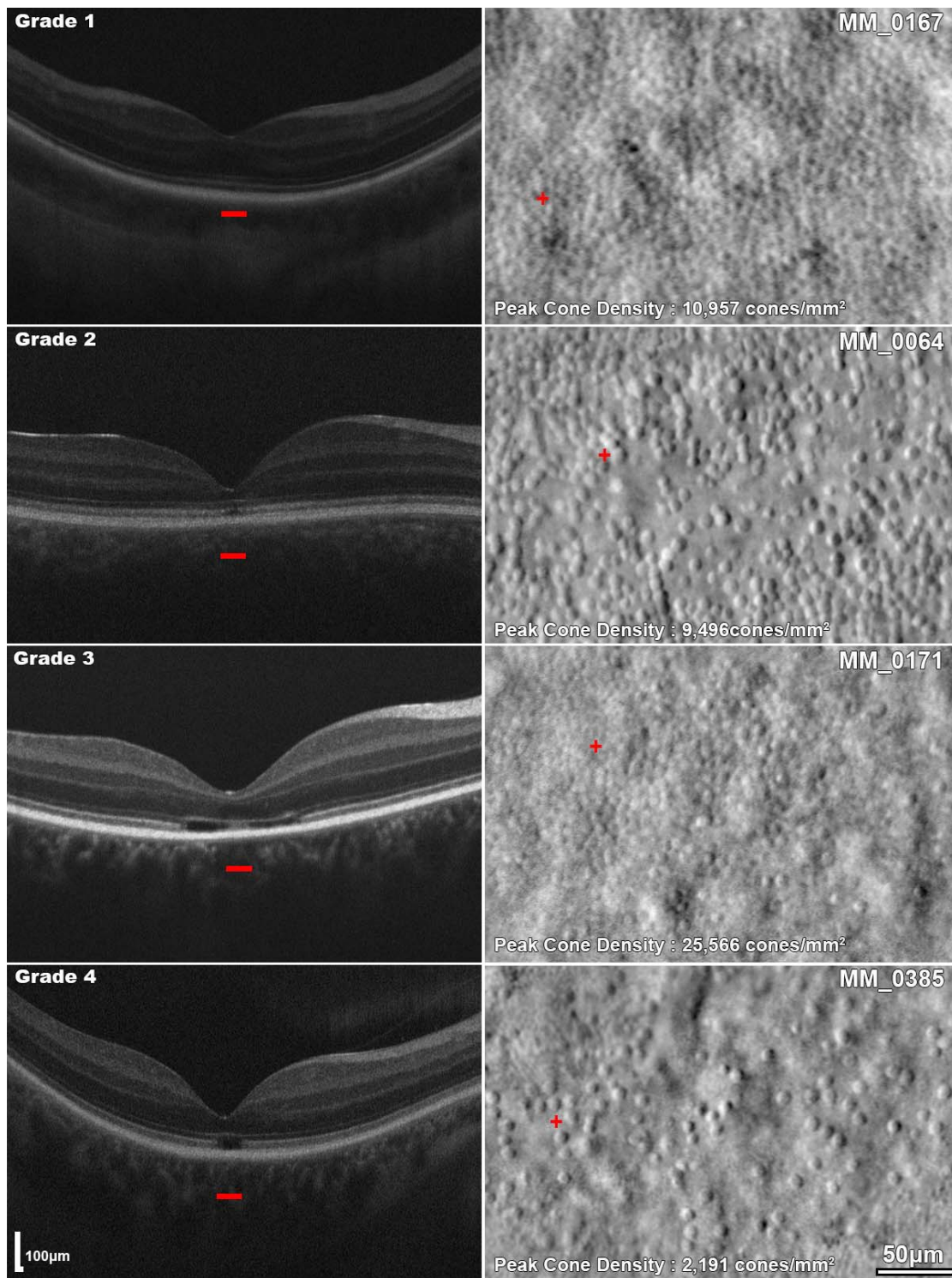
FIGURE 2. Remnant cone structure in different OCT EZ grades of *CNGA3*-associated ACHM. *Left column*: horizontal transfoveal OCT scans of four subjects with different OCT EZ grades. Grade 1: Continuous EZ, grade 2: EZ disruption, grade 3: EZ absence, and grade 4: presence of a hyporeflective zone. The *red horizontal bars* mark the 300-μm area represented on the AOSLO images in the right column. *Right column*: split-detection AOSLO images for each subject. The *red cross* represents the location of peak foveal cone density.

TABLE 1. Demographics and Genotype Summary

			Variant 1		Variant 2	
Subject	**Sex**	**Age, y**	**cDNA Change**	**AA Change**	**cDNA Change**	**AA Change**
MM_0002*	F	41	1443-1444insC	Ile482His fs*6	1706G>A	Arg569His
MM_0008*	F	11	536T>A	Val179Asp	ND†	ND†
MM_0009*	F	14	536T>A	Val179Asp	ND†	ND†
MM_0014*	F	35	848G>A	Arg283Gln	667C>T	Arg223Trp
MM_0015*	F	28	848G>A	Arg283Gln	667C>T	Arg223Trp
MM_0016*	M	30	848G>A	Arg283Gln	667C>T	Arg223Trp
MM_0064*	F	23	1694C>T	Thr565Met	661C>T	Arg221Ter
MM_0164*	F	35	1641C>A	Phe547Leu	1641C>A	Phe547Leu
MM_0165*	M	13	1641C>A	Phe547Leu	1641C>A	Phe547Leu
MM_0167*	F	28	847C>T	Arg283Trp	1279C>T	Arg427Cys
MM_0168*	M	39	661C>T	Arg221Ter	848G>A	Arg283Gln
MM_0169*	M	14	485A>T	Asp162Val	485A>T	Asp162Val
MM_0170*	M	16	1642G>A	Gly548Arg	67C>T	Arg23Ter
MM_0171*	M	22	1001C>T	Ser334Phe	1360A>T	Lys454Ter
MM_0239*	M	37	848G>A	Arg283Gln	667C>T	Arg223Trp
MM_0251*	F	33	661C>T	Arg221Ter	661C>T	Arg221Ter
MM_0358	M	10	1641C>A	Phe547Leu	1641C>A	Phe547Leu
MM_0385	M	37	1228C>G	Arg410Trp	1228C>G	Arg410Trp
MM_0386	F	22	1580T>G	Leu527Arg	**1805G>A**	**Gly602Glu**
MM_0387	M	18	1580T>G	Leu527Arg	**1805G>A**	**Gly602Glu**
MM_0396	M	27	1306C>T	Arg436Trp	1279C>T	Arg427Cys
MM_0397	M	18	1306C>T	Arg436Trp	1279C>T	Arg427Cys
MM_0398	F	14	811C>T	Pro271Ser	829C>T	Arg277Cys
MM_0412	M	13	**1286T>C**	**Val429Ala**	**608G>A**	**Trp203Cys fs*29**
MM_0418	M	18	661C>T	Arg221Ter	661C>T	Arg221Ter
MM_0445	M	10	1641C>A	Phe547Leu	1641C>A	Phe547Leu
MM_0446*	F	50	67C>T	Arg23Ter	67C>T	Arg23Ter
JC_0578	M	32	1687C>T	Arg563Cys	778G>A	Asp260Asn
JC_0615	M	43	1306C>T	Arg436Trp	1306C>T	Arg436Trp
JC_0626	F	20	1641C>A	Phe547Leu	1641C>A	Phe547Leu
JC_0674	M	46	985G>T	Gly329Cys	985G>T	Gly329Cys
JC_0698	M	43	848G>A	Arg283Gln	1228C>T	Arg410Trp
JC_1240*	F	24	1351dupG	Val451Gly fs*3	1279C>T	Arg427Cys
JC_10008	F	12	829C>T	Arg277Cys	1641C>A	Phe547Leu
JC_10069*	M	18	847C>T	Arg283Trp	542A>G	Tyr181Cys
KS_10088*	F	64	450-1G>A	splice defect	1557G>A	Met519Ile
KS_10337‡	F	17	940_942delATC	Ile314del	1114C>T	Pro372Ser
JC_10551	M	10	1228C>T	Arg410Trp	**1319G>C**	**Trp440Ser**

In bold are the previously unreported sequence variants. ND, no data; F, female; M, male; AA, amino acid.
* Subjects previously reported.[19,20,30,33,76]
† Only one variant identified. Phenotype consistent with *CNGA3*-ACHM. No variants found in *CNGB3*.
‡ Subject harbors an additional variant in *CNGB3*: c.473C>A: p.Pro158His.

analyzable split-detection AOSLO, as metrics of remnant foveal cone packing.

Statistical Methods

Statistical analysis was performed with GraphPad Prism (version 8.0.1; GraphPad Software, San Diego, CA, USA). Parametric and nonparametric tests were used depending on normality tests (Shapiro-Wilk normality test), as well as correlation coefficients (either Pearson or Spearman, respectively).

RESULTS

Demographics

Thirty-eight subjects from 30 families were recruited, including 21 males (55%) and 17 females (45%), with a mean (range, ±SD) age, in years, of 25.9 (10–64, ±13.1). Ten subjects were children (under 16 years old), with a mean (range, ±SD) age, in years, of 12.1 (10–14, ±1.7). Demographics are summarized in Table 1.

Genetics

All subjects harbored likely disease-causing sequence variants in *CNGA3*, with 12 (32%) being homozygous and 24 (63%) compound heterozygous. The remaining two of the 38 subjects (MM_0008 and MM_0009, siblings) harbored a single heterozygous variant and were shown to have no variants in *CNGB3*, with a typical ACHM phenotype. In one subject (KS_10337), an additional *CNGB3* sequence variant was identified. In total, 33 different variants were observed in our cohort, with 4 not previously reported to the best of our knowledge (Table 1, marked in bold).

The majority of the variants resulted in single amino acid substitutions (25/33, 76%). In addition, three different nucleotide changes introduced translation termination codons, three more introduced frame shift changes, one was an intronic change disrupting splicing, and one was a 3-base pair deletion. The most common was c.1641C>A (p.Phe547Leu; 11 alleles, three pedigrees), followed by c.848G>A (p.Arg283Gln; six alleles, three pedigrees) and c.661C>T (p.Arg221Ter; six alleles, four pedigrees). All sequence variants and protein alterations are reported in Table 1.

Ocular Examination

The mean (range, ±SD) axial length, in mm, for all 76 eyes was 24.21 (21.46–29.61, ±1.85); the mean (±SD) axial length, in mm, for the right and left eyes was 24.25 (±1.91) and 24.17 (±1.81), respectively. No significant difference was noted between eyes ($P = 0.344$, Wilcoxon matched-pairs test). The mean (±SD) axial length, in mm, for male and female subjects was 24.07 (±1.66) and 24.46 (±2.21), respectively. No significant difference in axial length was noted between sexes ($P = 0.586$, Mann-Whitney test). The age, in years, of male and female subcohorts also did not differ significantly ($P = 0.508$, Mann-Whitney test), with mean (±SD) 24.48 (±12.28) and 27.71 (±14.29), respectively.

BCVA was documented for 32 of 38 subjects. One subject (MM_0386) had congenital light perception in one eye, without the presence of other sequence variants or eye disease after thorough clinical investigation, had a BCVA of 0.98 logMAR in the other eye, and was excluded from further BCVA analysis. The mean (range, ±SD) BCVA was 0.87 logarithm of the minimum angle of resolution (LogMAR; 0.40–1.18, ±0.14). The mean (±SD) BCVA was 0.85 LogMAR (±0.14) and 0.88 LogMAR (±0.15) for right and left eyes, respectively; with no significant difference ($P = 0.327$, Wilcoxon matched-pairs test). BCVA and axial length for all subjects are shown in Table 2.

OCT Imaging

Retinal Morphology. OCT revealed a variable degree of disruption or loss of the foveal EZ and was graded as previously published (Fig. 2).[19] All subjects ($n = 38$) had the same EZ grade bilaterally. Four subjects (10.5%) had continuous EZ (grade 1), 19 subjects (50.0%) had EZ disruption (grade 2), 3 subjects (7.9%) had EZ absence (grade 3), and 12 subjects (31.6%) had presence of an HRZ (grade 4; Fig. 3A). None of the subjects included in the study had outer retinal atrophy including RPE loss (grade 5). In our cohort, the distribution of age was the same across the different OCT grades ($P = 0.086$, Kruskal-Wallis test).

Foveal ONL Thickness. The mean (±SD) ONL thickness, in μm, for grade 1 was 92.74 (±16.22), grade 2 was 78.69 (±25.12), grade 3 was 64.93 (±15.41), and grade 4 was 63.15 (±11.57). The mean (range, ±SD) ONL thickness, in μm, for all subjects was 74.18 (27.52–123.85, ± 21.80) (Table 2, Fig. 3B). Previously reported mean ± SD from unaffected controls for ONL thickness is 110.6 ± 15.7 μm, with an $n = 38$ (mean age ± SD; 28.8 ± 10.9 years);[46] these values are significantly higher than our reported values for *CNGA3*-ACHM ($P < 0.0001$, t = 8.37, df = 74). ONL thickness at the fovea was measured with standard OCT. The residual Henle fiber layer (HFL) may have been included within the ONL measurement, but given the foveal location, only a small degree of error is expected. The HFL comprised only 17.5% of the measured HFL+ONL thickness (range, 11.4%–24.8%) at the fovea of healthy controls.[47] Due to a small number of subjects with grade 1 and 3 EZ, the data were not further statistically analyzed. Grade 2 subjects had a significantly greater ONL

thickness than grade 4 subjects ($P = 0.054$, t = 2.005, df = 29). Despite the trend toward decreasing ONL thickness with increasing EZ grade (i.e., increasing EZ disruption/loss), there is overlap between grades (Fig. 3C).

Foveal Hypoplasia. Hypoplasia was observed bilaterally in 25 subjects (65.8%) to variable degrees. There was no significant difference in ONL thickness between individuals with foveal hypoplasia and those with normal excavation of inner retinal layers ($P = 0.861$, Mann-Whitney test) (Table 2). No association was found between foveal hypoplasia and EZ grade ($P = 0.199$, chi-square test). Subjects with foveal hypoplasia ($n = 19$, BCVA = 0.86 LogMAR, SD = 0.13) had similar BCVA compared to subjects without foveal hypoplasia ($n = 12$, mean BCVA = 0.87 LogMAR, SD = 0.19; $P = 0.924$, t = 0.096, df = 29).

Photoreceptor Mosaic Assessed With AOSLO Imaging

AOSLO imaging was attempted in all recruited subjects ($n = 38$). Eighteen (47.4%) had good-quality images and met the aforementioned eligibility criteria. If bilateral data were available, the eye with the better image quality was included for further analysis in all subjects. Foveal hypoplasia did not correlate with successful AOSLO imaging ($P = 0.506$, Fisher's exact test), with the main limiting factor in AOSLO acquisition being the severity of nystagmus.

Peak Foveal Cone Density. The mean peak foveal cone density was 19,844 cones/mm^2, ranging from 6,574 cones/mm^2 to 54,785 cones/mm^2 (Table 2). There was marked variability between subjects with a SD of 13,046 cones/mm^2 (Table 2); however, as expected, these values do not overlap with previously reported normative values (range, 84,733–247,064 cones/mm^2).[48,49]

There was no significant difference in peak foveal cone density between individuals with foveal hypoplasia and those with normal excavation of inner retinal layers ($P = 0.974$, t = 0.0334, df = 16), a finding that has also been previously reported for *CNGB3*-ACHM.[36] Peak foveal cone density was available for two subjects with EZ grade 1 and only for one subject with EZ grade 3 and, therefore, were excluded from statistical evaluation. There was no significant difference in peak foveal cone density between individuals with a grade 2 EZ and those with a grade 4 EZ ($P = 0.129$, t = 1.619, df = 13). All peak cone density data are plotted in Figure 3D. In contrast, in the aforementioned *CNGB3* study, peak foveal cone density, and EZ grade were significantly associated.[36] Peak foveal cone density and ONL thickness were not correlated ($P = 0.927$, r = 0.023, Pearson correlation), in keeping with the previous *CNGB3* study.[36] There was a weak negative association between age and peak foveal cone density ($P = 0.102$, r = −0.397, Pearson correlation) (Figs. 3E).

Intercell Distance. The mean (μ) and SD (σ) of the ICD for each subject ($n = 18$) was evaluated, as well as the CV (CV = σ/μ), to measure the overall variability of ICD independent of the value, which, as expected, varied widely. The mean ICD (range, ±SD), in μm, was 13.40 (6.07–27.86, ±5.74). As expected, the mean ICD in *CNGA3*-ACHM was greater ($P < 0.0001$, Mann-Whitney test) than in unaffected controls ($n = 6$; ICD mean ± SD, 3.61 ± 0.22 μm).[36]

Our cohort had a CV (mean ± SD) of 0.32 ± 0.1, which was significantly higher ($P = 0.0002$, t = 4.537, df = 22) than healthy controls ($n = 6$; CV mean ± SD, 0.13 ± 0.014).[36]

Structural Disease Symmetry. In seven subjects, bilateral OCT and AOSLO imaging data were obtained (one male, six females; age (mean ± SD), 32.6 ± 11.9 years) (Table 2; Fig. 4). All subjects had the same bilateral EZ grade; three subjects had grade 2 and four had grade 4. Six (85.7%) subjects had bilateral

TABLE 2.   Retinal Phenotype–Optical Coherence Tomography and Adaptive Optics Imaging Summary

Subject	Eye	Axial Length, mm	BCVA, LogMAR	Foveal Hypoplasia	EZ Grade	ONL Thickness, μm	PFD, Cones/mm^2	ICD Mean, μm	ICD SD (σ)	ICD CV
MM_0002	OD	24.4	0.74	Yes	2	76.67	16,801	13.04	3.61	0.28
	OS	24.38	0.82	Yes	2	82.56	13,148	12.85	3.46	0.27
MM_0008	OD	23.14	1.06	No	2	72.74	ND	ND	ND	ND
	OS	23.08	1	No	2	ND	ND	ND	ND	ND
MM_0009	OD	21.53	0.98	No	2	72.74	22,644	9.31	2.63	0.28
	OS	21.46	1	No	2	ND	ND	ND	ND	ND
MM_0014	OD	25.33	0.76	Yes	4	73.12	6,574	24.35	7.43	0.31
	OS	25.54	0.72	Yes	4	75.48	7,305	25.24	8.06	0.32
MM_0015	OD	25.2	0.84	Yes	4	60.94	24,835	15.66	6.57	0.42
	OS	24.75	0.78	Yes	4	49.15	32,140	10.19	4.32	0.42
MM_0016	OD	24.38	0.9	Yes	4	ND	ND	ND	ND	ND
	OS	24.57	1.18	Yes	4	48.36	13,148	14.96	4.82	0.32
MM_0064	OD	22.46	0.78	No	2	27.52	9,496	11.41	2.88	0.25
	OS	22.51	0.8	No	2	29.49	7,305	11.10	2.12	0.19
MM_0164	OD	25.56	0.92	Yes	2	123.85	ND	ND	ND	ND
	OS	25.83	0.8	Yes	2	ND	ND	ND	ND	ND
MM_0165	OD	24.99	0.84	Yes	4	60.94	16,801	13.36	4.12	0.31
	OS	24.88	0.7	Yes	4	ND	ND	ND	ND	ND
MM_0167	OD	24.96	1.06	No	1	ND	ND	ND	ND	ND
	OS	25.04	1.16	No	1	110.09	10,957	12.89	6.62	0.51
MM_0168	OD	28.74	0.8	No	2	68.80	ND	ND	ND	ND
	OS	28.24	0.92	No	2	ND	ND	ND	ND	ND
MM_0169	OD	24.77	0.74	No	1	92.39	ND	ND	ND	ND
	OS	24.19	1.12	No	1	ND	ND	ND	ND	ND
MM_0170	OD	21.79	0.78	Yes	2	55.04	27,757	8.42	1.74	0.21
	OS	21.71	0.76	Yes	2	ND	ND	ND	ND	ND
MM_0171	OD	22.87	0.7	Yes	3	47.18	25,566	12.18	6.01	0.49
	OS	22.74	0.76	Yes	3	ND	ND	ND	ND	ND
MM_0239	OD	23.33	0.72	Yes	4	66.84	16,070	18.00	6.56	0.36
	OS	23.23	0.9	Yes	4	58.40	13,148	17.09	6.44	0.38
MM_0251	OD	29.61	0.72	Yes	3	72.73	ND	ND	ND	ND
	OS	29.51	0.66	Yes	3	ND	ND	ND	ND	ND
MM_0358	OD	23.62	0.82	No	2	94.36	ND	ND	ND	ND
	OS	23.52	0.88	No	2	ND	ND	ND	ND	ND
MM_0385	OD	24.41	0.8	No	4	ND	ND	ND	ND	ND
	OS	24.35	0.8	No	4	39.32	2,191	27.86	13.81	0.50
MM_0386	OD	24.1	0.98	Yes	2	94.36	13,148	12.93	3.85	0.30
	OS	23.38	LP	Yes	2	ND	ND	ND	ND	ND
MM_0387	OD	22.89	0.84	Yes	4	74.7	ND	ND	ND	ND
	OS	22.88	0.88	Yes	4	ND	ND	ICD	ND	ND
MM_0396	OD	23.63	1	Yes	2	ND	ND	ND	ICD	ICD
	OS	23.6	1.02	Yes	2	90.12	ND	ND	ND	ND
MM_0397	OD	22.15	0.96	No	2	96.33	ND	ND	ND	ND
	OS	21.92	0.96	No	2	ND	ND	ND	ND	ND
MM_0398	OD	23.18	1	Yes	2	53.08	20,453	8.68	1.69	0.20
	OS	23.49	1.12	Yes	2	49.15	19,722	8.44	1.42	0.17
MM_0412	OD	23.36	1	Yes	2	57.01	ND	ND	ND	ND
	OS	23.37	1.02	Yes	2	ND	ND	ND	ND	ND
MM_0418	OD	24.2	0.9	No	2	64.04	ND	ND	ND	ND
	OS	24.36	0.8	No	2	ND	ND	ND	ND	ND
MM_0445	OD	22.72	1	Yes	2	62.91	ND	ND	ND	ND
	OS	22.87	1	Yes	2	ND	ND	ND	ND	ND
MM_0446	OD	24.81	0.76	Yes	4	70.76	6,574	18.90	6.45	0.34
	OS	24.91	0.7	Yes	4	73.32	5,844	20.69	7.18	0.35
JC_0578	OD	27.21	ND	Yes	2	79.87	ND	ND	ND	ND
	OS	26.47	ND	Yes	2	ND	ND	ND	ND	ND
JC_0615	OD	25.63	ND	No	3	ND	ND	ND	ND	ND
	OS	25.65	ND	No	3	74.88	ND	ND	ND	ND
JC_0626	OD	28.85	ND	Yes	2	114.82	ND	ND	ND	ND
	OS	28.35	ND	Yes	2	ND	ND	ND	ND	ND
JC_0674	OD	25.02	ND	Yes	4	ND	ND	ND	ND	ND
	OS	24.36	ND	Yes	4	64.90	ND	ND	ND	ND

TABLE 2. Continued

Subject	Eye	Axial Length, mm	BCVA, LogMAR	Foveal Hypoplasia	EZ Grade	ONL Thickness, μm	PFD, Cones/mm²	ICD Mean, μm	ICD SD (σ)	ICD CV
JC_0698	OD	24.27	0.9	Yes	4	ND	ND	ND	ND	ND
	OS	23.79	0.9	Yes	4	73.63	ND	ND	ND	ND
JC_1240	OD	21.62	0.4	No	4	64.90	ND	ND	ND	ND
	OS	21.72	0.54	No	4	ND	ND	ND	ND	ND
JC_10008	OD	22.62	ND	Yes	4	71.14	ND	ND	ND	ND
	OS	22.76	ND	Yes	4	ND	ND	ND	ND	ND
JC_10069	OD	23.13	0.8	Yes	2	67.39	40,906	7.10	1.29	0.18
	OS	23.59	0.8	Yes	2	ND	ND	ND	ND	ND
KS_10088	OD	25.19	ND	Yes	2	123.55	21,183	11.56	3.80	0.33
	OS	25.34	ND	Yes	2	ND	ND	ND	ND	ND
KS_10337	OD	23.29	1.0	No	1	71.14	54,785	6.07	1.28	0.21
	OS	23.78	0.88	No	1	ND	ND	ND	ND	ND
JC_10551	OD	22.46	0.9	Yes	1	ND	ND	ND	ND	ND
	OS	22.39	0.9	Yes	1	97.34	ND	ND	ND	ND

ND, no data; BCVA, best corrected visual acuity; EZ, ellipsoid zone; PFD, peak foveal cone density; ICD, intercell distance; SD, standard deviation; CV, coefficient of variation; ONL, outer nuclear layer; LP, light perception.

foveal hypoplasia. The absolute difference in ONL thickness between right and left eyes (mean ± SD) was 4.16 ± 2.31 μm. ONL thickness did not differ significantly between eyes ($P = 0.754$, t = 0.329, df = 6), with mean (±SD) ONL thickness, in μm, of 59.03 (±17.92) and 59.65 (±18.68) for right and left eyes, respectively.

Peak foveal cone density was also comparable bilaterally ($P = 0.829$, t = 0.225, df = 6), with mean ± SD of 14,400 ± 7,078 cones/mm² and 14,087 ± 9,304 cones/mm² for the right and left eyes, respectively. The difference in peak foveal cone density (mean ± SD) between eyes was 2,609 ± 2,380 cones/mm². ICDs were also similar bilaterally ($P = 0.496$, t = 0.725, df = 6), with mean ± SD of 15.72 ± 5.25 μm and 15.09 ± 6.16 μm for right and left eyes, respectively. The mean ± SD of CV was 0.31 ± 0.07 and 0.30 ± 0.09 for right and left eyes, respectively; indicating that mosaic topography was similar between eyes ($P = 0.448$, t = 0.812, df = 6).

Intrafamilial Variability. We recruited three pairs of siblings (Tables 1 and 2; MM_0008-MM_0009, MM_0386-MM_0387, and MM_0396-MM_0397), four siblings (MM_0014, MM_0015, MM_0016, and MM_0239), and a mother with two sons (MM_0164, MM_0165, and MM_0445, respectively) (Tables 1, 2). Two pairs of siblings (MM_0008-MM_0009 and MM_0396-MM_0397) had the same EZ grade and comparable ONL thickness (mean difference among siblings of 3 μm). AOSLO data were analyzable in only one of those four subjects. The four siblings (MM_0014, MM_0015, MM_0016, and MM_0239) had substantial variability of their cone mosaics even though their EZ grade was the same (grade 4). AOSLO imaging was available for all four siblings (three bilaterally) (Fig. 5A). The cone mosaic was variably disrupted, without any specific pattern among these subjects. Despite the differences in remnant cone structure, the subject with the lowest peak foveal cone density (right/left eye, 6,574 and 7,305 cones/mm², respectively) had the best BCVA among his siblings. For the last pair of siblings and the family with the three affected members, only one cone mosaic per family could be analyzed and no conclusion about the intrafamilial variability of their mosaics could be drawn. However, in both families there was a notable difference in the disruption of the photoreceptor mosaic on OCT; the two siblings MM_0386 and MM_0387 had grade 2 and 4 EZs, respectively, and from the other pedigree, two subjects had grade 2 and one grade 4 EZs

(Fig. 5B). BCVA was comparable among these subjects (Table 2).

DISCUSSION

The foveal cone mosaic in *CNGA3*-ACHM was irregular, variably disrupted, and showed significantly lower peak foveal cone density than unaffected individuals. A striking structural feature that was clear in our cohort was the irregular size and shape of the remnant inner segments (Figs. 2, 4, 5). Irregularities in shape and size have been described in the limited number of histology reports in patients with ACHM.[50-52] In all three reports, the patients were well phenotyped but not genotyped, because it was before the discovery of the ACHM genes. The unusual shape of the inner segments was attributed to the presence of ectopic nuclei.[50-52] Using OCT imaging, Genead et al.[29] previously reported a substantial variation in phenotype even in subjects with the same genotype. Our subjects with *CNGA3*-ACHM had a significantly thinner ONL than unaffected individuals, although there was significant variability between subjects. No correlation was found between peak foveal cone density and ONL thickness. Our findings are in keeping with previous reports for *CNGB3*-ACHM.[36] There was a broad range of cone densities within each EZ grade. This dissociation between OCT and peak foveal cone density highlights the value of AOSLO for patient stratification and evaluation of retinal potential for therapy trials. Notable examples are subjects MM_0015 (Fig. 5) and MM_0171 (Fig. 2), who despite being graded as 4 and 3, respectively, have a peak foveal cone density higher than the average for the cohort and may thus be good candidates for an intervention. However, it is still unclear what should be considered as a threshold and which metric will best correlate with outcome. We will certainly be in a better position to address these questions when the results of the current gene therapy trials using AOSLO are released.

Despite the vast variability among subjects, interocular symmetry was observed in all aspects examined, including axial length, BCVA, EZ grade, presence of foveal hypoplasia, ONL thickness, peak foveal cone density, and mosaic geometry (ICD and CV). This information is of high value both for eye selection for an intervention, as well as for longitudinal evaluation of the outcome of ongoing and upcoming trials, in which the nontreated eye can serve as a control. Overall,
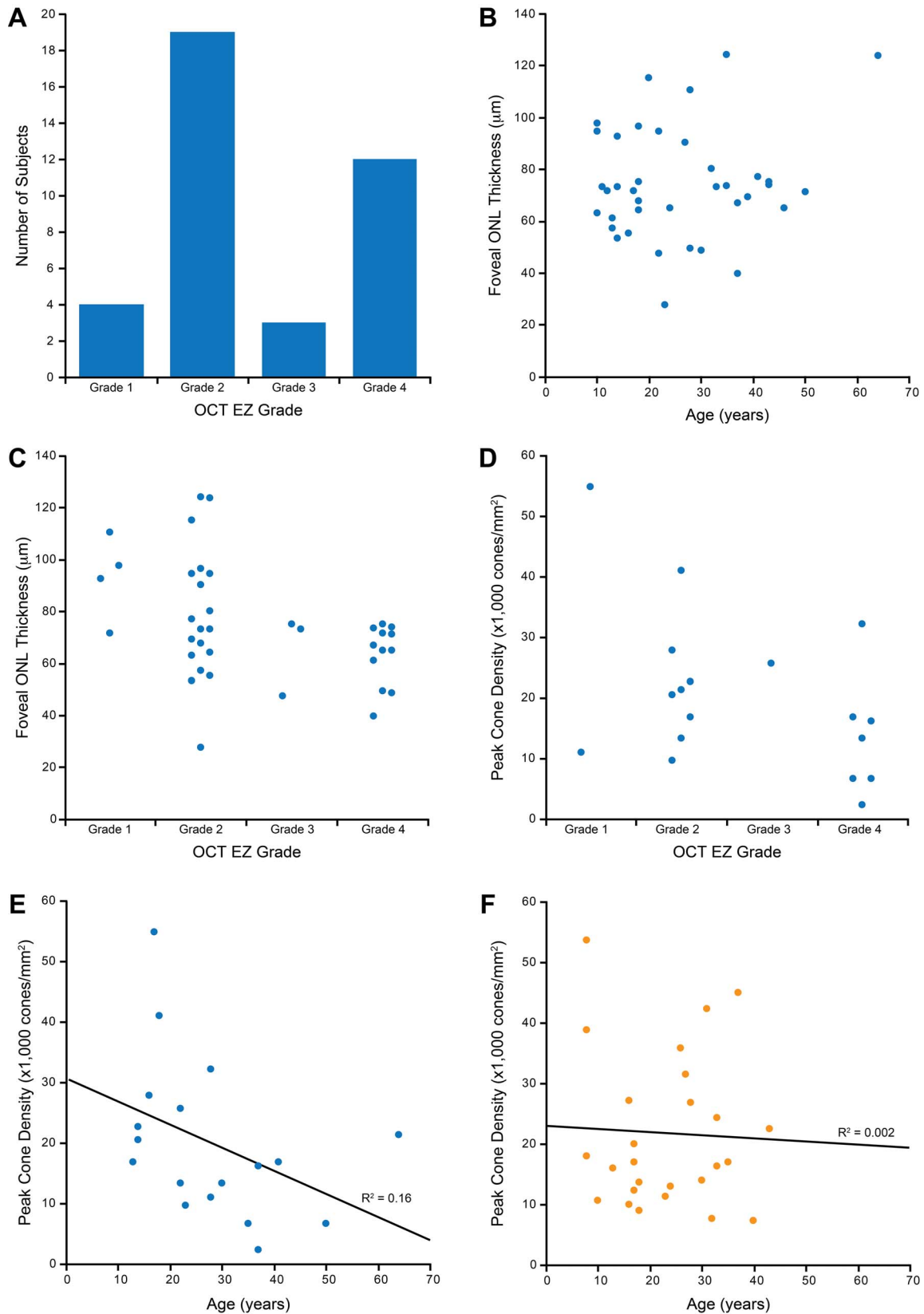
FIGURE 3. Results summary and graphical representation. (**A**) Distribution of our cohort according to OCT grading, with the vast majority having either grade 2 or 4. (**B**) Scatter plot of ONL thickness and age. No correlation was found. (**C**) Stacked scatterplot of ONL thickness and OCT EZ grade, showing the vast variability within and between grades, as well as a trend of decreasing ONL thickness with increasing grade. (**D**) Stacked scatterplot of peak cone density and OCT EZ showing the overlap between grades. In (**C**) and (**D**), individual data points within each EZ grade are displaced horizontally for better visibility. (**E**) Peak cone densities of all subjects with *CNGA3*-ACHM included in this study plotted against age. (**F**) Peak cone densities of all subjects with *CNGB3*-ACHM previously reported by Langlo et al.[36] plotted against age on the same scale as (**E**). The *CNGA3* cohort plotted on (**E**) shows a weak negative correlation between peak cone density and age (Pearson r = −0.397, P = 0.102).
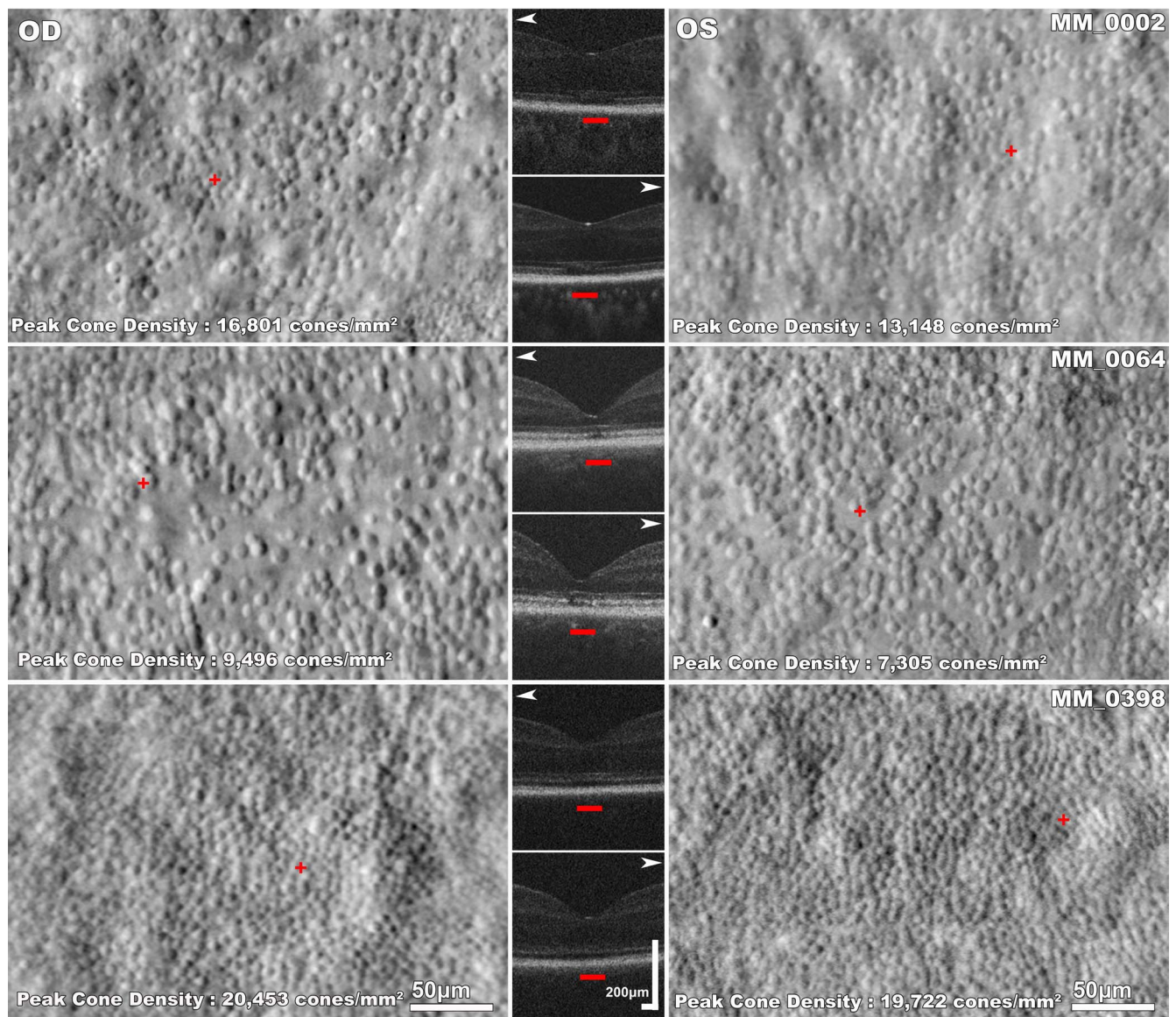
FIGURE 4. Disease symmetry in *CNGA3*-associated ACHM. *Left* and *right column*: split-detection AOSLO images of the right and left eye respectively of three subjects with *CNGA3*-ACHM. *Middle column*: horizontal transfoveal OCT scans of the same subjects. *White arrowheads* point to the respective AOSLO image. The *red horizontal bars* mark the 300-μm area represented in the AOSLO images. There is substantial variability in foveal photoreceptor mosaic between the three subjects. There are structural similarities in the mosaic pattern of the right and left eyes of each subject; MM_0002 and MM_0064 have noncontiguous sparse foveal mosaics and MM_0398 has a relatively contiguous mosaic. MM_0002 has OCT grade 4 bilaterally with foveal hypoplasia. MM_0064 and MM_0398 have EZ grade 2 bilaterally.

CNGA3-ACHM appears to be a structurally symmetric disease in keeping with previous literature that did not use AOSLO.[19] Many subjects had a variable degree of foveal hypoplasia, which is consistent with previous studies both for *CNGA3* and *CNGB3*.[19,29,36] No difference in BCVA was noted between eyes with and without foveal hypoplasia, in contrast to previous studies that suggested better[19] or worse[40] BCVA in the presence of foveal hypoplasia. As previously suggested by Thomas et al.,[53] incomplete centrifugal displacement of the inner retinal layers is a common finding. No current literature has investigated the mechanism/molecular basis of foveal hypoplasia in ACHM.

The majority of subjects had missense sequence variants, suggesting little tolerance for substitutions, in agreement with the high degree of evolutionary conservation of the *CNGA3* gene.[17] There was marked genetic variability, although no

genotype-phenotype correlation could be observed. There is a notable intrafamilial variability of the cone mosaic topography and of the peak foveal cone density (Fig. 5). EZ grade and ONL thickness were far less sensitive in detecting structural differences, which again illustrates a disconnect between OCT and AOSLO. In other cases, intrafamilial variability was also clear on OCT. The observed marked intrafamilial variability in *CNGA3*-ACHM shows a lack of genotype-phenotype correlation in ACHM caused by *CNGA3* variants, with specific genetic variants not being predictive of remnant cone structure.

Thiadens et al.[54] and Thomas et al.[40] suggested an age-dependent ONL thinning.[54] In contrast, Sundaram et al.[19] and Aboshiha et al.[20] did not identify such a relationship. Langlo et al.[35] in a longitudinal *CNGB3* assessment reported increasing ONL thickness over time (6–26 months). In our cohort, no
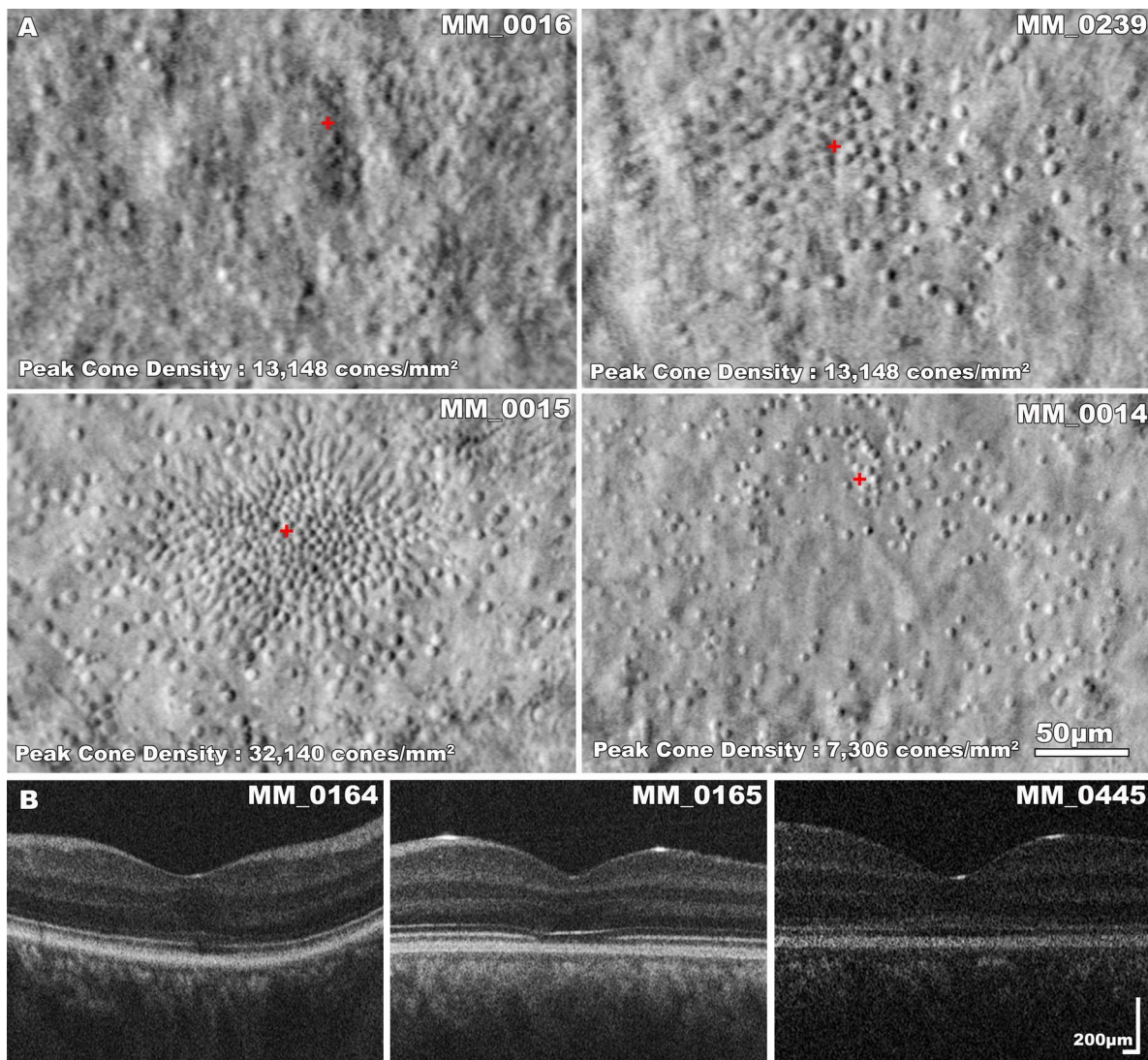
FIGURE 5. Intrafamilial variability in *CNGA3*-associated ACHM. (**A**) Split-detection AOSLO images of four siblings with *CNGA3*-ACHM. MM_0016 (VA, 0.86 LogMAR) and MM_0239 (VA, 0.90 LogMAR) are males, 30 and 37 years old, respectively. MM_0015 (VA, 0.84 LogMAR) and MM_0014 (VA, 0.74 LogMAR) are females, 28 and 35 years old, respectively. There is substantial variability in foveal photoreceptor mosaic across the four subjects, which is independent of sex or age. All four siblings have EZ grade 4 bilaterally with foveal hypoplasia. The identification of 40 cones within the 55×55-μm sampling window resulted in a density of 13,148 cones/mm^2 for both siblings, MM_0016 and MM_0239. However, other parameters such as the ICD were different, reflecting the geometry of cones over the foveal center; MM_0239 had greater mean ICD due to a sparser mosaic in the inferior fovea. The *red cross* marks the location of peak foveal cone density. (**B**) Transfoveal OCT scans of subjects MM_0164, MM_0165, and MM_0445, from a single family. Female subject MM_0164 (VA, 0.92 LogMAR, mother of the male siblings MM_0165 and MM_0445) has a better preserved EZ than the 25 year younger subject MM_0165 (VA, 0.84 LogMAR); and subject MM_0445 (VA, 1.0 LogMAR) has a nearly continuous EZ.

correlation between ONL thickness and age was found. Previously Sundaram et al.[19] suggested a wider window of opportunity for intervention in ACHM and no age-dependent association in retinal structure disruption, identifying the need for the specific measurement of remnant photoreceptor structure, with SD-OCT and AOSLO imaging for stratification of patients and evaluating intervention efficacy.

While there was no association between age and ONL thickness, we observed a weak negative association between age and peak foveal cone density (Fig. 3E) as well as age and EZ grade. While a similar cross-sectional study of *CNGB3*-ACHM showed an association between age and EZ grade,[36] that study reported no relationship between age and peak foveal cone density (Fig. 3F). In the aforementioned *CNGB3* study, the subcohort imaged successfully with AOSLO had a mean age ($\pm$SD), in years, of 23.4 ($\pm$10.3) and our cohort had a mean age

($\pm$SD) of 28.3 ($\pm$13.8), with the age distribution not differing significantly among the two studies ($P = 0.186$, t = 1.35, df = 42). The mean peak foveal cone density is also similar between the two studies ($P = 0.71$, Mann-Whitney test). No distinguishing phenotypic characteristics could be identified for our *CNGA3* genotype compared to the current literature for *CNGB3*. Similarity in *CNGA3*- and *CNGB3*-associated ACHM was also observed in the data from microperimetry, fundus autofluorescence, and OCT by Aboshiha et al.[20] and Sundaram et al.[19]

The proteins encoded by *CNGA3* and *CNGB3* have been well characterized, and differences in their function may relate to the age-dependent decline that we observed in our *CNGA3* cohort, in contrast to the previously well characterized *CNGB3* cohort using the same methodology.[36] It has been shown than the α subunits expressed by *CNGA3* are responsible for the ion-

conducting activity of the cation channel and the β subunits modulate the activity.[55,56] It has also been shown in $CNGA3^{-/-}$ mice that the loss of *CNGA3* expression impairs the correct localization of cone opsins as well as the expression of other proteins of the visual cycle, with this inducing apoptotic cell death in cones.[57] In the $CNGB3^{-/-}$ mice, a downregulation of *CNGA3* gene expression of ~90% has been observed.[58] The residual *CNGA3* expression may account for the preservation of remnant cones in *CNGB3*-ACHM. By extension, the complete absence/greater reduction of *CNGA3* expression may lead to an age-dependent decline of remnant cones in *CNGA3*-ACHM (as we observe), also bearing in mind that α subunits in vitro can form channels in the absence of β subunits, a property not shared by β subunits.[59]

However, given the limitations of the cross-sectional nature of this study, a longitudinal assessment and further evaluation of the progressive or stationary nature of *CNGA3*-ACHM would be invaluable. Longitudinal studies are necessary to properly address the question of cone loss over time. The lack of studies using AOSLO in age-matched subjects in order to investigate possible age-related decline in healthy eyes makes it challenging to put our findings in context. The current literature in healthy eyes is inconclusive for possible age-dependent changes in peak foveal cone density, either using histology or AO retinal imaging.[60–63] Nevertheless, in agreement with previous reports,[29,36,59] all of the subjects in the present study had remnant cone structure (across the entire age range studied). However, no functional assessment of those cones was possible, which will be interesting both in terms of disease natural history and for assessing the outcomes of any intervention.[64] Despite the observed decrease of peak foveal cone density with age, there were several notable exceptions, with high peak foveal cone density in older subjects and no clear age cutoff identified. This shows that despite the statistical relationship, there is still great variability in cone populations across all ages and, thus, the need for longitudinal studies.

Analyzable AOSLO was achieved in only 18/38 subjects and can be attributed to nystagmus in the vast majority of subjects, as well as to poor optical media and high myopia in some. Nystagmus (or absence thereof) has not been correlated with either lower or higher remnant photoreceptor structure in the current literature. Nystagmus in ACHM has previously been reported to improve over time,[65,66] and given the stationary, or only slowly progressive, natural history of the condition, our reported peak foveal cone densities are likely representative of the *CNGA3* genotype. In this study, subjects with strong nystagmus, in which AOSLO was not analyzable, had a range of EZ grades on OCT, further supporting that nystagmus is not representative of the structural severity of the disease or remnant cone architecture. We anticipate that the challenge nystagmus poses to imaging quality will be ameliorated with the use of eye tracking in the near future.[67–69] In addition to the low successful acquisition rate, several other factors should be taken into account when considering using AOSLO in research studies or even clinical practice; acquisition time is considerable and requires the participation of two investigators for our custom-built system, with processing, montaging, and analysis being substantial bottlenecks. Newly developed software for simplifying the steps of the process are of high value for the field, such as montaging[45,70] and cone counting.[71–75]

In conclusion, *CNGA3*-ACHM retinas can be successfully imaged with split-detection AOSLO, with most findings in keeping with *CNGB3*-ACHM. To the best of our knowledge, we report the largest *CNGA3*-ACHM study to include split-detection AOSLO imaging. There is a need for prospective longitudinal studies of large cohorts of molecularly confirmed *CNGA3* subjects to improve our understanding of the cellular natural history.[76] Given the large variability in cone mosaics, subjects with ACHM should be assessed on an individual basis for selection in future and ongoing clinical trials.

References

1. Aboshiha J, Dubis AM, Carroll J, Hardcastle AJ, Michaelides M. The cone dysfunction syndromes. *Br J Ophthalmol*. 2016; 100:115–121.

2. Hirji N, Aboshiha J, Georgiou M, Bainbridge J, Michaelides M. Achromatopsia: clinical features, molecular genetics, animal models and therapeutic options. *Ophthalmic Genet*. 2018;39: 149–157.

3. Maguire J, McKibbin M, Khan K, Kohl S, Ali M, McKeefry D. *CNGB3* mutations cause severe rod dysfunction. *Ophthalmic Genet*. 2017;39:108–114.

4. Khan NW, Wissinger B, Kohl S, Sieving PA. *CNGB3* achromatopsia with progressive loss of residual cone function and impaired rod-mediated function. *Invest Ophthalmol Vis Sci*. 2007;48:3864–3871.

5. Thiadens AA, Roosing S, Collin RW, et al. Comprehensive analysis of the achromatopsia genes *CNGA3* and *CNGB3* in progressive cone dystrophy. *Ophthalmology*. 2010;117:825–830.e1.

6. Wissinger B, Jagle H, Kohl S, et al. Human rod monochromacy: linkage analysis and mapping of a cone photoreceptor expressed candidate gene on chromosome 2q11. *Genomics*. 1998;51:325–331.

7. Wissinger B, Gamer D, Jagle H, et al. *CNGA3* mutations in hereditary cone photoreceptor disorders. *Am J Hum Genet*. 2001;69:722–737.

8. Mayer AK, Van Cauwenbergh C, Rother C, et al. *CNGB3* mutation spectrum including copy number variations in 552 achromatopsia patients. *Hum Mut*. 2017;38:1579–1591.

9. Kohl S, Baumann B, Rosenberg T, et al. Mutations in the cone photoreceptor G-protein alpha-subunit gene *GNAT2* in patients with achromatopsia. *Am J Hum Genet*. 2002;71: 422–425.

10. Aligianis IA, Forshew T, Johnson S, et al. Mapping of a novel locus for achromatopsia (ACHM4) to 1p and identification of a germline mutation in the alpha subunit of cone transducin (GNAT2). *J Med Genet*. 2002;39:656–660.

11. Kohl S, Zobor D, Chiang WC, et al. Mutations in the unfolded protein response regulator ATF6 cause the cone dysfunction disorder achromatopsia. *Nat Genet*. 2015;47:757–765.

12. Kohl S, Coppieters F, Meire F, et al. A nonsense mutation in *PDE6H* causes autosomal-recessive incomplete achromatopsia. *Am J Hum Genet*. 2012;91:527–532.

13. Fesenko EE, Kolesnikov SS, Lyubarsky AL. Induction by cyclic GMP of cationic conductance in plasma membrane of retinal rod outer segment. *Nature*. 1985;313:310–313.

14. Yu WP, Grunwald ME, Yau KW. Molecular cloning, functional expression and chromosomal localization of a human homolog of the cyclic nucleotide-gated ion channel of retinal cone photoreceptors. *FEBS Lett*. 1996;393:211–215.

15. Wissinger B, Muller F, Weyand I, et al. Cloning, chromosomal localization and functional expression of the gene encoding the alpha-subunit of the cGMP-gated channel in human cone photoreceptors. *Eur J Neurosci*. 1997;9:2512–2521.

16. Michaelides M, Hunt DM, Moore AT. The cone dysfunction syndromes. *Br J Ophthalmol*. 2004;88:291–297.

17. Johnson S, Michaelides M, Aligianis IA, et al. Achromatopsia caused by novel mutations in both *CNGA3* and *CNGB3*. *J Med Genet*. 2004;41:e20.

18. Zobor D, Werner A, Stanzial F, et al. The clinical phenotype of *CNGA3*-related achromatopsia: pretreatment characterization in preparation of a gene replacement therapy trial. *Invest Ophthalmol Vis Sci*. 2017;58:821–832.

19. Sundaram V, Wilde C, Aboshiha J, et al. Retinal structure and function in achromatopsia: implications for gene therapy. *Ophthalmology*. 2014;121:234–245.

20. Aboshiha J, Dubis AM, Cowing J, et al. A prospective longitudinal study of retinal structure and function in achromatopsia. *Invest Ophthalmol Vis Sci*. 2014;55:5733–5743.

21. Georgiou M, Kalitzeos A, Patterson EJ, Dubra A, Carroll J, Michaelides M. Adaptive optics imaging of inherited retinal diseases. *Br J Ophthalmol*. 2018;102:1028–1035.

22. Roorda A, Williams DR. The arrangement of the three cone classes in the living human eye. *Nature*. 1999;397:520–522.

23. Dubra A, Sulai Y, Norris JL, et al. Noninvasive imaging of the human rod photoreceptor mosaic using a confocal adaptive optics scanning ophthalmoscope. *Biomed Opt Express*. 2011;2:1864–1876.

24. Rossi EA, Chung M, Dubra A, Hunter JJ, Merigan WH, Williams DR. Imaging retinal mosaics in the living eye. *Eye (Lond)*. 2011;25:301–308.

25. Liang J, Williams DR, Miller DT. Supernormal vision and high-resolution retinal imaging through adaptive optics. *J Opt Soc Am A Opt Image Sci Vis*. 1997;14:2884–2892.

26. Roorda A, Duncan JL. Adaptive optics ophthalmoscopy. *Ann Rev Vis Sci*. 2015;1:19–50.

27. Roorda A, Williams DR. Optical fiber properties of individual human cones. *J Vis*. 2002;2:404–412.

28. Carroll J, Choi SS, Williams DR. In vivo imaging of the photoreceptor mosaic of a rod monochromat. *Vision Res*. 2008;48:2564–2568.

29. Genead MA, Fishman GA, Rha J, et al. Photoreceptor structure and function in patients with congenital achromatopsia. *Invest Ophthalmol Vis Sci*. 2011;52:7298–7308.

30. Dubis AM, Cooper RF, Aboshiha J, et al. Genotype-dependent variability in residual cone structure in achromatopsia: toward developing metrics for assessing cone health. *Invest Ophthalmol Vis Sci*. 2014;55:7303–7311.

31. Merino D, Duncan JL, Tiruveedhula P, Roorda A. Observation of cone and rod photoreceptors in normal subjects and patients using a new generation adaptive optics scanning laser ophthalmoscope. *Biomed Opt Express*. 2011;2:2189–2201.

32. Ueno S, Nakanishi A, Kominami T, et al. In vivo imaging of a cone mosaic in a patient with achromatopsia associated with a *GNAT2* variant. *Jpn J Ophthalmol*. 2017;61:92–98.

33. Scoles D, Sulai YN, Langlo CS, et al. In vivo imaging of human cone photoreceptor inner segments. *Invest Ophthalmol Vis Sci*. 2014;55:4244–4251.

34. Abozaid MA, Langlo CS, Dubis AM, Michaelides M, Tarima S, Carroll J. Reliability and repeatability of cone density measurements in patients with congenital achromatopsia. *Adv Exp Med Biol*. 2016;854:277–283.

35. Langlo CS, Erker LR, Parker M, et al. Repeatability and longitudinal assessment of foveal cone structure in *CNGB3*-associated achromatopsia. *Retina*. 2017;37:1956–1966.

36. Langlo CS, Patterson EJ, Higgins BP, et al. Residual foveal cone structure in *CNGB3*-associated achromatopsia. *Invest Ophthalmol Vis Sci*. 2016;57:3984–3995.

37. Scoles D, Flatter JA, Cooper RF, et al. Assessing photoreceptor structure associated with ellipsoid zone disruptions visualized with optical coherence tomography. *Retina*. 2016;36:91–103.

38. Thevenaz P, Ruttimann UE, Unser M. A pyramid approach to subpixel registration based on intensity. *IEEE Trans Image Process*. 1998;7:27–41.

39. Huang Y, Cideciyan AV, Papastergiou GI, et al. Relation of optical coherence tomography to microanatomy in normal and rd chickens. *Invest Ophthalmol Vis Sci*. 1998;39:2405–2416.

40. Thomas MG, Kumar A, Kohl S, Proudlock FA, Gottlob I. High-resolution in vivo imaging in achromatopsia. *Ophthalmology*. 2011;118:882–887.

41. Staurenghi G, Sadda S, Chakravarthy U, Spaide RF. Proposed lexicon for anatomic landmarks in normal posterior segment spectral-domain optical coherence tomography: the IN*OCT consensus. *Ophthalmology*. 2014;121:1572–1578.

42. Dubra A, Sulai Y. Reflective afocal broadband adaptive optics scanning ophthalmoscope. *Biomed Opt Express*. 2011;2:1757–1768.

43. Salmon AE, Cooper RF, Langlo CS, Baghaie A, Dubra A, Carroll J. An automated reference frame selection (ARFS) algorithm for cone imaging with adaptive optics scanning light ophthalmoscopy. *Trans Vis Sci Tech*. 2017;6(2):9.

44. Dubra A, Harvey Z. *Registration of 2D Images From Fast Scanning Ophthalmic Instruments*. Berlin, Heidelberg: Springer Berlin Heidelberg; 2010:60–71.

45. Davidson B, Kalitzeos A, Carroll J, et al. Fast adaptive optics scanning light ophthalmoscope retinal montaging. *Biomed Opt Express*. 2018;9:4317–4328.

46. Mastey R, Litts KM, Langlo CS, et al. Interocular symmetry and repeatability of foveal outer nuclear layer thickness in congenital achromatopsia. *bioRxiV*. 2018:367813. https://doi.org/10.1101/367813.

47. Lee DJ, Woertz EN, Visotcky A, et al. The Henle fiber layer in albinism: comparison to normal and relationship to outer nuclear layer thickness and foveal cone density. *Invest Ophthalmol Vis Sci*. 2018;59:5336–5348.

48. Wilk MA, McAllister JT, Cooper RF, et al. Relationship between foveal cone specialization and pit morphology in albinism. *Invest Ophthalmol Vis Sci*. 2014;55:4186–4198.

49. Zhang T, Godara P, Blanco ER, et al. Variability in human cone topography assessed by adaptive optics scanning laser ophthalmoscopy. *Am J Ophthalmol*. 2015;160:290–300.e1.

50. Harrison R, Hoefnagel D, Hayward JN. Congenital total color blindness: a clincopathological report. *Arch Ophthalmol*. 1960;64:685–692.

51. Glickstein M, Heath GG. Receptors in the monochromat eye. *Vision Res*. 1975;15:633–636.

52. Falls HF, Wolter JR, Alpern M. Typical total monochromacy. A histological and psychophysical study. *Arch Ophthalmol*. 1965;74:610–616.

53. Thomas MG, Kumar A, Mohammad S, et al. Structural grading of foveal hypoplasia using spectral-domain optical coherence

tomography a predictor of visual acuity? *Ophthalmology.* 2011;118:1653–1660.

54. Thiadens AA, Slingerland NW, Roosing S, et al. Genetic etiology and clinical consequences of complete and incomplete achromatopsia. *Ophthalmology.* 2009;116:1984–1989.e1.

55. Zagotta WN, Siegelbaum SA. Structure and function of cyclic nucleotide-gated channels. *Ann Rev Neurosci.* 1996;19:235–263.

56. Gerstner A, Zong X, Hofmann F, Biel M. Molecular cloning and functional characterization of a new modulatory cyclic nucleotide-gated channel subunit from mouse retina. *J Neurosci.* 2000;20:1324–1332.

57. Michalakis S, Geiger H, Haverkamp S, Hofmann F, Gerstner A, Biel M. Impaired opsin targeting and cone photoreceptor migration in the retina of mice lacking the cyclic nucleotide-gated channel CNGA3. *Invest Ophthalmol Vis Sci.* 2005;46:1516–1524.

58. Ding XQ, Harry CS, Umino Y, Matveev AV, Fliesler SJ, Barlow RB. Impaired cone function and cone degeneration resulting from CNGB3 deficiency: down-regulation of CNGA3 biosynthesis as a potential mechanism. *Hum Mol Genet.* 2009;18:4770–4780.

59. Nishiguchi KM, Sandberg MA, Gorji N, Berson EL, Dryja TP. Cone cGMP-gated channel mutations and clinical findings in patients with achromatopsia, macular degeneration, and other hereditary cone diseases. *Hum Mut.* 2005;25:248–258.

60. Curcio CA, Millican CL, Allen KA, Kalina RE. Aging of the human photoreceptor mosaic: evidence for selective vulnerability of rods in central retina. *Invest Ophthalmol Vis Sci.* 1993;34:3278–3296.

61. Song H, Chui TY, Zhong Z, Elsner AE, Burns SA. Variation of cone photoreceptor packing density with retinal eccentricity and age. *Invest Ophthalmol Vis Sci.* 2011;52:7376–7384.

62. Chui TY, Song H, Clark CA, Papay JA, Burns SA, Elsner AE. Cone photoreceptor packing density and the outer nuclear layer thickness in healthy subjects. *Invest Ophthalmol Vis Sci.* 2012;53:3545–3553.

63. Curcio CA. Photoreceptor topography in ageing and age-related maculopathy. *Eye (Lond)* 2001;15:376–383.

64. Domdei N, Domdei L, Reiniger JL, et al. Ultra-high contrast retinal display system for single photoreceptor psychophysics. *Biomed Opt Express.* 2018;9:157–172.

65. Kohl S, Jagle H, Wissinger B. Achromatopsia. In: Adam MP, Ardinger HH, Pagon RA, et al., eds. *GeneReviews*. Seattle, WA: University of Washington, Seattle; 1993.

66. Zobor D, Zobor G, Kohl S. Achromatopsia: on the doorstep of a possible therapy. *Ophthalmic Res.* 2015;54:103–108.

67. Sheehy CK, Tiruveedhula P, Sabesan R, Roorda A. Active eye-tracking for an adaptive optics scanning laser ophthalmoscope. *Biomed Opt Express.* 2015;6:2412–2423.

68. Privitera CM, Sabesan R, Winter S, Tiruveedhula P, Roorda A. Eye-tracking technology for real-time monitoring of transverse chromatic aberration. *Optics Lett.* 2016;41:1728–1731.

69. Tam J, Roorda A. Speed quantification and tracking of moving objects in adaptive optics scanning laser ophthalmoscopy. *J Biomed Opt.* 2011;16:036002.

70. Chen M, Cooper RF, Han GK, Gee J, Brainard DH, Morgan JI. Multi-modal automatic montaging of adaptive optics retinal images. *Biomed Opt Express.* 2016;7:4899–4918.

71. Davidson B, Kalitzeos A, Carroll J, et al. Automatic cone photoreceptor localisation in healthy and stargardt afflicted retinas using deep learning. *Sci Rep.* 2018;8:7911.

72. Bergeles C, Dubis AM, Davidson B, et al. Unsupervised identification of cone photoreceptors in non-confocal adaptive optics scanning light ophthalmoscope images. *Biomed Opt Express.* 2017;8:3081–3094.

73. Cunefare D, Langlo CS, Patterson EJ, et al. Deep learning based detection of cone photoreceptors with multimodal adaptive optics scanning light ophthalmoscope images of achromatopsia. *Biomed Opt Express.* 2018;9:3740–3756.

74. Cunefare D, Fang L, Cooper RF, Dubra A, Carroll J, Farsiu S. Open source software for automatic detection of cone photoreceptors in adaptive optics ophthalmoscopy using convolutional neural networks. *Sci Rep.* 2017;7:6620.

75. Cunefare D, Cooper RF, Higgins B, et al. Automatic detection of cone photoreceptors in split detector adaptive optics scanning light ophthalmoscope images. *Biomed Opt Express.* 2016;7:2036–2050.

76. Hirji N, Georgiou M, Kalitzeos A, et al. Longitudinal assessment of retinal structure in achromatopsia patients with long-term follow-up. *Invest Ophthalmol Vis Sci.* 2018;59:5735–5744.